Journal of
Materials Chemistry C

ROYAL SOCIETY
OF CHEMISTRY

PAPER

View Article Online
View Journal | View Issue

Check for updates

Cite this: J. Mater. Chem. C, 2020, 8, 3491

Coaxially enhanced photocarrier transport of a highly oriented Cu_2ZnSnS_4/ZnO photodetector through the nanoconfinement effect†

Wen Li, ‡ Da Xiong,‡ Meilin Xie, Chao Luo, Xiankan Zeng, Yue Gao, Bolin Guo, Cheng Yan, Fengjun Chun, Zhihao Zhu, Xiaoqiang Fan, Weili Deng and Weiqing Yang *

Received 15th November 2019, Accepted 27th January 2020

DOI: 10.1039/c9tc06275k

rsc.li/materials-c

Nontoxic self-powered ZnO-based photodetectors are highly desired to meet the great demand for sensing, communication, and imaging applications, while directionally manipulating the confined photocarrier transport is critical to the enhancement in the photodetection performance. Herein, we demonstrated a highly *c*-axis-oriented Cu_2ZnSnS_4/ZnO (CZTS/ZnO) photodetector with coaxially enhanced photocarrier transport. This CZTS/ZnO photodetector delivers remarkable 31 times higher photocurrent mainly ascribed to the coaxially enhanced photocarrier transport in the vertically directed ZnO arrays through the nanoconfinement effect along with the substantially enhanced incident photon absorption of length-optimized ZnO nanorods (NRs). Furthermore, this photodetector delivers a high responsivity of 1.1 μA W^{-1}, fast rise time of 600 ms, and decay time of 600 ms as well as good stability with no distinct photocurrent decay after 2500 cycles. This study will open up a coaxially enhanced photocarrier transport way to substantially improve the photodetection performance and may promote the development of next-generation optoelectronic devices.

Introduction

Considering the human health and environmental hazards, nontoxic photodetectors are highly desirable in various potential applications such as target detection, light vision, military surveillance and nondestructive image technology.[1–4] However, most photodetectors usually employ highly toxic compounds containing toxic elements, such as cadmium (Cd) and lead (Pb), restricting their large-scale commercial prospects to some extent.[5–12] In this regard, there are some impressive works on nontoxic ZnO-based p–n junction photodetectors with a good ultraviolet (UV) response owing to their wide bandgap ($\approx$3.3 eV) and high exciton binding energy ($\approx$60 meV).[13–17] You *et al.* fabricated $CsPbBr_3$/ZnO heterostructure photodetectors, which exhibited a high on/off ratio (4104), high photoresponsivity (4.25 A W^{-1}) and fast response time (210 ms); the recombination of photoexcited electron–hole pairs in the perovskites was limited and the interfacial charge transfer from perovskites to ZnO was efficient. This p-type material contains a toxic element (Pb), which hinders the wide applications of such a device.[18] Thus, completely replacing toxic p-type materials with nontoxic elements is a pressing need to fundamentally address this matter. Li *et al.* fabricated self-powered visible-blind UV photodetectors based on nontoxic p-NiO nanoflakes/n-ZnO NR arrays. The MgO interfacial layer could modify the surface defect states of ZnO NRs and reduce the recombination of photogenerated carriers at the heterojunction interface.[19] Ghamgosar *et al.* proposed a nontoxic ZnO–Co_3O_4 core–shell nanowire heterojunction photodetector and the responsivity (R) was 21.80 mA W^{-1}; a thin layer of the Al_2O_3 buffer layer was introduced to inhibit charge recombination.[20] Fortunately, there have been some efforts to investigate a nontoxic p-type Cu_2ZnSnS_4 (CZTS) semiconductor for photovoltaic applications with the highest efficiency of 12.6%.[21–25] This p-type CZTS is a direct bandgap semiconductor with the advantages of a large optical absorption coefficient ($\approx 10^5$ cm^{-1}), earth-abundant elements, and outstanding environmental and electrical stabilities.[26] More importantly, its conduction and valence band positions match with those of ZnO, which is beneficial for the separation of photogenerated electron–hole pairs. Therefore, this nontoxic p-type CZTS holds great promise in building a nontoxic CZTS/ZnO photodetector.

Key Laboratory of Advanced Technologies of Materials (Ministry of Education), School of Materials Science and Engineering, Southwest Jiaotong University, Chengdu 610031, China. E-mail: wqyang@swjtu.edu.cn; Fax: +86-028-87601211; Tel: +86-028-87601211

† Electronic supplementary information (ESI) available: Detailed experimental procedures and characterization and additional figures including XRD, cross-sectional SEM images, photoreponse of CZTS/ZnO photodetectors and PL spectrum of the CZTS/ZnO heterojunction. See DOI: 10.1039/c9tc06275k

‡ These authors contributed equally to this work.

Under conventional conditions, the wurtzite-structured ZnO belongs to a hexagonal crystal system and has an asymmetric structure with *c*-axis orientation. In particular, highly oriented arrays of one-dimensional (1D) ZnO show attractive characteristics for certain applications, which can integrate large numbers of nanorod (NR)/nanowire energy harvesters into a single power source. Furthermore, the 1D ZnO nanostructures show a high aspect ratio, quantum confinement, and direct path for electrons, promoting a higher electron diffusion coefficient of the ZnO arrays as compared to nanoparticle films with multiple trapping/de-trapping events occurring within the grain boundaries.[27] Their uniquely preferential *c*-axis orientation along the polar $\langle 0001 \rangle$ direction is usually employed for the piezo-phototronic photodetectors.[28–31] Wang *et al.* reported a metal–semiconductor–metal (MSM) photodetector using a ZnO wire with *c* axis orientation for the detection of sub-μW cm^{-2} UV light, which could be increased dramatically by the piezo-phototronic effect, and the study provided an in-depth understanding about the physical mechanism of the coupling of piezoelectric, optical, and semiconducting properties.[32] Fang *et al.* successfully synthesized a 1D binary ZnS/ZnO biaxial nanobelt photodetector, which showed a hetero-crystalline structure with ZnO(0001)/ZnS(0001) interfaces; this photodetector is suitable for UV-A (320–400 nm) light detection and has a fast response speed (<0.3 s).[33] Furthermore, Dang *et al.* reported a *c*-axis-oriented ZnO/Gr hybrid-channel FET device with a higher response than ZnO nanoparticles/Gr through the quantum confinement effect of ZnO NRs. Due to the quantum confinement effect, the bandgap of ZnO NRs was narrower than that of the ZnO nanoparticles, and the free electron concentration in the conduction band of ZnO NRs under UV exposure was higher than that in the ZnO nanoparticles.[34] Meanwhile, the low dimensionality of the ZnO nanowires endows them with carrier confinement-induced band-gap tunability. The surface states on the ZnO nanowires result in appreciable energy band bending in the radial direction of the ZnO nanowires, which can lead to the separation of photo-generated electrons and holes in the radial direction, thus dramatically prolonging the carrier lifetime.[35] At the same time, the reduced dimensionality of the active area in the nanowire devices shortens the carrier transit time, which results in photoconductive gain as high as $G = 2 \times 10^8$ in ZnO nanowire photodetectors.[36] This confinement effect can result in high photosensitivity. Recently, Hassan *et al.* constructed a self-powered *c*-axis-oriented ZnO NR array/p-Si UV detector with higher sensitivity and faster response-recovery time under UV light at zero-bias voltage.[37] Hence, utilizing highly *c*-axis-oriented 1D ZnO NR arrays for coaxial photocarrier transportation will provide a new strategy for constructing a nontoxic CZTS/ZnO photodetector with fully enhanced photodetection performance.

Herein, we demonstrate a nontoxic self-powered CZTS/ZnO photodetector based on vertically directed ZnO NR arrays. Through the nanoconfinement effect, the 1D ZnO NR arrays can provide numerous direct electron-transmitting channels for coaxially enhanced photocarrier transport. This CZTS/ZnO photodetector delivers remarkable 31 times enhanced photocurrent as compared to the ZnO nanoparticles. Also, this photodetector presents an impressive responsivity of 1.1 $\mu A\ W^{-1}$, fast rise time of 600 ms, and decay time of 600 ms as well as good stability with no distinct photocurrent decay after 2500 cycles. This strategy evidently suggests a new route for designing and constructing materials with superior photocarrier transport in optoelectronic devices and remarkably promotes nontoxic photodetectors for practical applications.

Experimental section

The synthesis of CZTS nanocrystals (NCs): in a typical synthesis, 1.5 mmol of $Cu(CH_3COO)_2{\cdot}H_2O$ (99.0%, Aladdin), 0.75 mmol of $Zn(CH_3COO)_2{\cdot}2H_2O$ (99.0%, Aladdin), 0.75 mmol of $SnCl_2$ (98.0%, Aladdin), and 10 mL of oleylamine (80–90%, Aladdin) were added into a 100 mL three-neck flask. All metal salts were completely dissolved at 130 °C under vacuum and the mixture was degassed for 30 minutes. When the temperature was raised to 225 °C, 3 mL of 1 M solution of sulfur in oleylamine was injected. After the injection, the temperature was maintained at 225 °C for 30 minutes to complete the reaction and finally, the color of the solution turned black. After being cooled to room temperature, the products were centrifuged and washed with toluene and isopropanol several times. After centrifugation, the final precipitate was redispersed in toluene to form a stable ink solution.

The growth of ZnO NR array: as the ZnO seed layer can help to reduce the mismatch between the NRs and the substrate, we first deposited the ZnO seed layer on an ITO substrate using the radio frequency magnetron sputtering technology. Then, the ZnO NR array was prepared by a chemical bath deposition method. The ZnO seed/ITO glasses were immersed in the growth solution containing hexamethylenetetramine (HMTA) and $Zn(NO_3)_2{\cdot}6H_2O$. The concentration of this growth solution was 0.1 M and different lengths of ZnO NR arrays were obtained by changing the reaction time at 85 °C. Finally, the products were dried at 85 °C and stored for later use. The reaction times for the hydrothermal process were 1 h, 2 h, 3 h, 4 h, 5 h and 6 h. The ZnO layer obtained after 1 h was labeled as poorly oriented ZnO, while the ZnO NR array obtained after 5 h was named as highly oriented ZnO.

The preparation of a photodetector: the CZTS NC ink was applied directly on the surface of ZnO NR array by spin-coating. Then, the Ag electrode was sputtered on the heterojunction as the top electrode to form the sandwich structure.

Characterization

The morphologies of both the CZTS NCs and the ZnO NR layer were characterized by a field emission scanning electron microscope (FESEM JSM7800F). The transmission electron microscopy (TEM) images of CZTS NCs were taken with a JEOL JEM 2100F field emission transmission electron microscope at 200 kV. Raman spectra were recorded on a Renishaw inVia Raman microscope with the 514 nm line of an Ar ion laser as an excitation source. Absorption spectra were collected using a

Shimadzu UV-2600 spectrophotometer. The crystal structure of the film was examined by X-ray diffraction (XRD X'pert Powder) at 40 kV and 40 mA using Cu Ka radiation. The volt-ampere characteristics of the photodetectors were obtained on a Keithley 4200 semiconductor testing system, while the photoelectric performance was recorded on the Stanford SR570 Preamplifier. The light source was a controlled laser by the function signal generator.

Results and discussion

Fig. 1a schematically illustrates the structure of the CZTS/ZnO photodetector; p-type CZTS NCs were mounted on the surface of highly *c*-axis-oriented ZnO NR arrays to build a p–n junction. Once CZTS NCs and ZnO closely contacted each other in the dark, electron transfer occurred across the interface from ZnO to CZTS but holes were transferred in the opposite direction until their Fermi levels became aligned. These photocarriers will intrinsically result in the generation of a built-in potential ΔE (about 1.8 eV) and thus band bending at the interface, as shown in Fig. 1b.[38] When the energy of incident photons is above the bandgap of semiconductors, photoexcited electron–hole pairs will be spontaneously formed. Under the built-in electric field force, these electron–hole pairs will be immediately separated in opposite directions at the p–n interfaces, which naturally results in the generation of photocurrent. In this case, the vertically aligned ZnO NR array with a high aspect ratio can effectively provide a direct electron transport path for promoting more efficient electron transportation, which directly drives these generated photocarriers to the external ITO electrode along the highly *c*-axis-oriented ZnO NRs through the nanoconfinement effect. Such a highly *c*-axis-oriented ZnO NR tunnel will be substantially beneficial for coaxially enhanced photocarrier transportation. Hence, this highly oriented vertical structure is conducive to remarkably enhance the photocarrier transport for boosting the photoresponse. From the top-view SEM image of the vertically aligned ZnO NR arrays, the diameters of ZnO NRs are found to be in the range of 80–180 nm (Fig. 1c). While from the top-view SEM image of CZTS/ZnO (Fig. 1d), it is clear that the CZTS NC thin film is tightly packed on the surface of the ZnO NR array. As shown in Fig. 1e, the ITO bottom electrode, vertically aligned ZnO NR arrays, both CZTS NC thin films and Ag upper electrode layer have been deposited in a sequence to build the highly *c*-axis-oriented CZTS/ZnO photodetector.

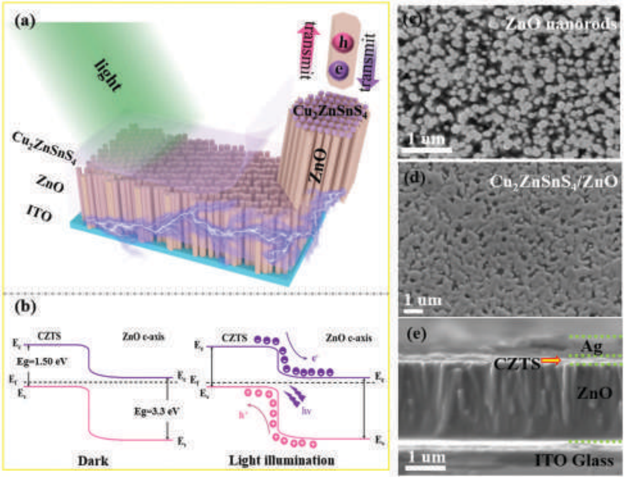

Fig. 1 CZTS/ZnO photodetector: (a) a schematic illustration of the fabricated photodetector, (b) energy band diagram of this photodetector in the dark and under light illumination, top-view SEM images of (c) pure ZnO NR film and (d) CZTS/ZnO film, (e) cross-sectional SEM image of fabricated photodetector.

Representative TEM and HRTEM micrographs were obtained to study the morphology and phase structure of the as-prepared CZTS NCs. These CZTS NCs have been slightly faceted to be an almost acorn-like shape (Fig. 2a). As shown in Fig. 2b, the HRTEM image of an individual NC exhibits distinct lattice fringes with a *d*-spacing value of 0.318 nm, which corresponds to the (112) plane in the kesterite structure of CZTS.[39] This kesterite crystalline structure of the as-synthesized CZTS NCs was further confirmed by three characteristic XRD diffraction peaks indexed to the (112), (220) and (312) planes of the kesterite structure (CZTS No. 26-0507), as depicted in Fig. S1 (ESI†). This XRD pattern also reveals no impurity peaks of CZTS NCs. To further evaluate phase purity, Raman spectroscopy was combined with XRD analysis. In Fig. 2c, the two broad Raman peaks at 335 and 289 cm^{-1} under an excited light of 514 nm agree well with the reported spectra of kesterite CZTS.[40] Importantly, no characteristic Raman peaks for CuS, ZnS, SnS_2 and Cu_2SnS_3 (472 cm^{-1}, 351 cm^{-1}, 315 cm^{-1} and 350 cm^{-1}, respectively) can be identified, ruling out the presence of these phases in the as-prepared CZTS NCs.[41] These pure phase kesterite CZTS NCs were directly deposited on a vertically aligned ZnO NR array to form a p–n heterojunction photodetector. In Fig. 2d, the EDS mapping results of the CZTS/ZnO surface obviously show the uniform element distribution (Cu, Zn, Sn, S and O) of the CZTS/ZnO thin film. Such high purity and excellent uniformity of the above-mentioned as-applied materials can guarantee the photodetection performance of the whole photodetector.

In order to deeply understand the nanoconfinement effect of a highly oriented ZnO NR array on the photocarrier transport of this device, two types of ZnO NR arrays were employed. One was a highly oriented ZnO NR array, while the other was a poorly oriented ZnO NR array. Fig. 2e displays the XRD patterns of the highly oriented ZnO NR arrays; a characteristic peak with higher intensity at 34.4° is observed for the highly oriented one, suggesting that ZnO NRs preferentially orient in the (002) direction parallel to the *c*-axis.[42] The optimally structure-oriented growth of the ZnO NR arrays is elaborated in Fig. S2 and S3 (ESI†). In order to prove that as the hydrothermal reaction time increases, ZnO NRs change from poorly oriented to highly oriented ZnO NRs, the diffraction intensity ratios of the (002) and (103) crystal planes were calculated to determine the orientation trend. As the reaction time increased, the ratios of I_{002}/I_{103} were 4.5, 24.4, 22.7, 36.5, 46.8 and 69.6. The ratio of the ZnO layer obtained after 1 h was too small, indicating that the ZnO layer obtained after 1 h did not have obvious growth orientation, and it was close to that of arbitrarily arranged nanoparticles. Hence, the ZnO layer obtained after 1 h was

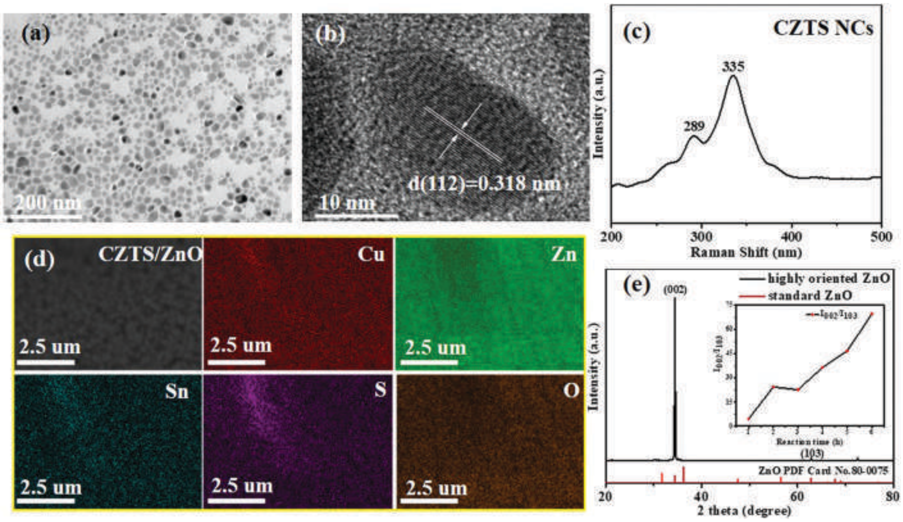

Fig. 2 Morphology and structure characterization of CZTS/ZnO photodetector: (a) the TEM image, (b) HRTEM image, (c) Raman spectrum of the as-synthesized kesterite CZTS NCs; (d) SEM micrograph and EDS mapping of CZTS/ZnO thin film surface; (e) XRD patterns of highly oriented ZnO and the inset is a function of reaction time and intensity ratio.

named as poorly oriented ZnO. The accurately modulated orientation of the ZnO NR array will be favorable to obtain thorough insights into its regulation mechanism of photocarrier transport.

As shown in Fig. 3a, both the CZTS/ZnO photodetectors with poorly oriented ZnO and highly oriented ZnO show obvious rectifying behavior, indicating the presence of a well-defined p–n junction at the interface between CZTS NCs and ZnO. The photovoltaic effect from the p–n junction can directly help the device to function as a self-powered photodetector operating at zero bias. However, as seen in Fig. 3b, the optimum self-powered photocurrent of the highly *c*-axis-oriented CZTS/ZnO photodetector at zero bias under 1.77 mW mm^{-2} illumination (λ = 450 nm) is as high as 11.64 nA, which is about 31 times higher than that of the poorly oriented CZTS/ZnO. Such remarkably elevated photodetector performance should be mainly ascribed to the following reasons: (i) the absorption coefficient of the highly *c*-axis-oriented CZTS/ZnO device with a thicker light conversion layer is higher than that of poorly oriented CZTS/ZnO (Fig. 3c). The poorly oriented ZnO NR array film is too short to absorb sufficient light and then, a large amount of light will rapidly dissipate through the film, leading to a substantial decrease in photocarriers. (ii) The adequately controlled length of the highly *c*-axis-oriented ZnO NR array can effectively ensure adequate carrier collection. The transfer distance of the photocarriers in this photodetector is closely related to the length of the ZnO NR array. If the length of the vertically aligned ZnO NR array is longer than the transfer distance of the photocarriers, the resulting nonradiative recombination will greatly lower its

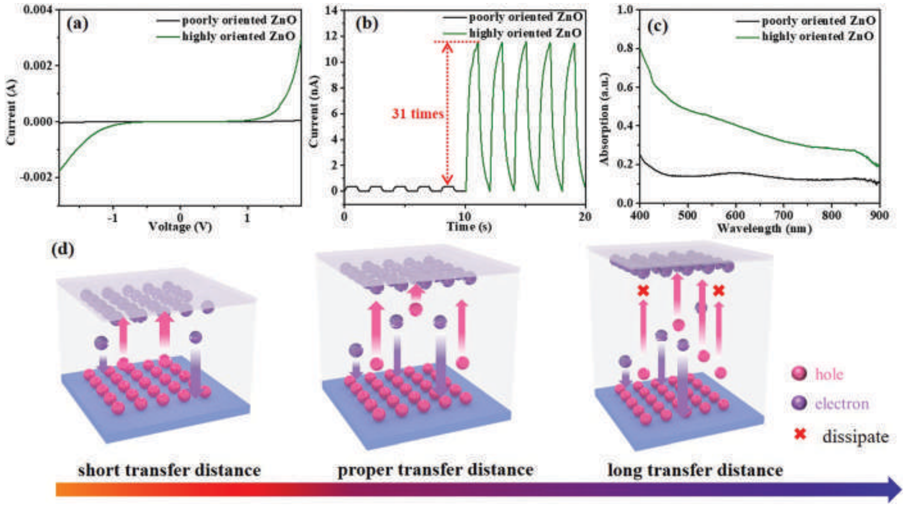

Fig. 3 The effect of ZnO on optical and electrical performance of CZTS/ZnO photodetectors: (a) *I*–*V* characteristic of photodetectors under dark conditions, (b) photoresponse behaviors under 450 nm (1.77 mW mm^{-2}) illumination without bias voltage, (c) absorption spectra, (d) the influence mechanism of ZnO structure orientation on the photocarrier transfer.

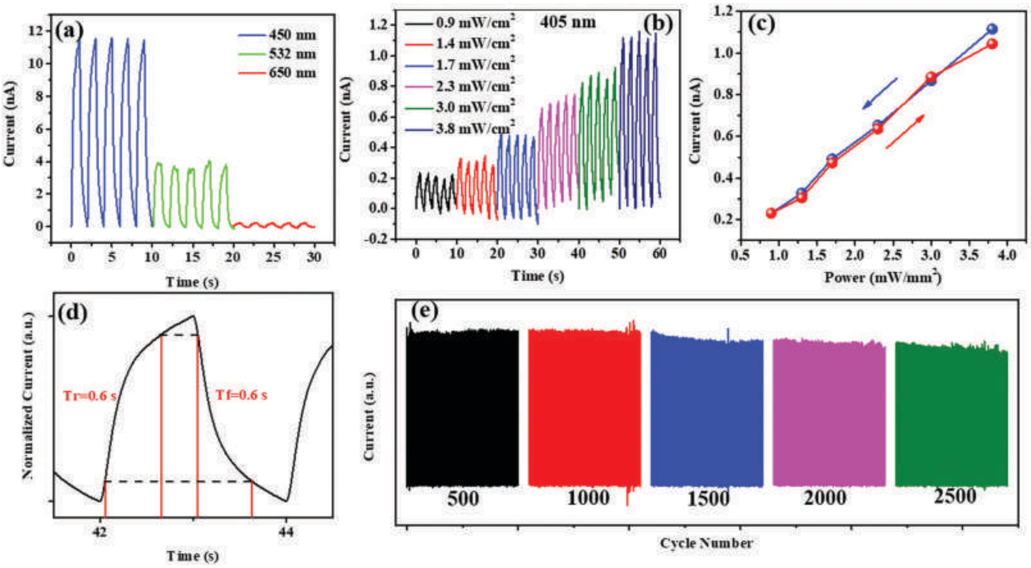

Fig. 4 Photoresponse and stability of CZTS/ZnO photodetectors: (a) photoresponse behavior of the photodetector under different light wavelengths of 450, 532 and 650 nm (1.77 mW mm^{-2}); (b) photoresponse behavior of the photodetector under 405 nm illuminations with different light intensities; (c) the photoresponse behaviour of the photodetector as a function of light intensity; (d) the response time of the designed photodetector; (e) cycling stability.

effective photocurrent number. Fig. 3d schematically illustrates the physical mechanism of photocarrier transmission with different lengths of the ZnO NR array. This mechanism can be evidently proved by fluctuant photocurrent with varying lengths of the ZnO NR array (Fig. S4, ESI†). (iii) The nanoconfinement effect of coaxially enhanced photocarrier transportation can effectively confine the axial transmission of photocarriers and lead to the separation of photo-generated electrons and holes in the radial direction. This path substantially cuts down photocarrier dissipation during the transmission process and dramatically prolongs the carrier lifetime. However, the poorly oriented ZnO NR array randomly stacks along the arbitrary orientation and then causes carrier recombination in this unconstrained transmission path, leading to a lower photoresponse with poor photocarrier transportation.

Fig. 4a presents the wavelength-dependent responsivity of the designed highly *c*-axis-oriented CZTS/ZnO photodetector under 450, 532 and 650 nm (1.77 mW mm^{-2}) illuminations. It was obvious that the photocurrent significantly decreased with the increase in the incident wavelength mainly due to the decrease in the long-wavelength light absorption capacity of the reduced photogenerated charge carriers. According to the current variations in one period (Fig. 4d), sharp current peaks are periodically generated under illumination; the response time ($\tau_{\rm res}$, the time required for the photocurrent to increase from 10% to 90%) of merely 600 ms and recovery time ($\tau_{\rm rec}$, the time required for the photocurrent to drop from 90% to 10%) of 600 ms are obtained. By adjusting the intensity of the incident 405 nm light from 0.9 to 3.8 mW cm^{-2}, the photocurrents gradually increased, as depicted in Fig. 4b. As shown in Fig. 4c, a nearly linear relationship between photocurrent and light intensity is observed under varied light intensities. Such excellent reproducibility of the linear dependence curve demonstrates its high stability. To understand the response mechanism of the photodetector, the room-temperature photoluminescence (PL) spectra acquired under 325 nm for the CZTS/ZnO heterojunction were investigated, as shown in Fig. S5 (ESI†). The near-band edge excitonic emission peak at 396 nm is due to the radiative recombination of electrons in the conduction band (CB) and holes in the valence band (VB). In addition, the peak in the visible region (465 nm) can be regarded as the defect-related emission (DLE) caused by the electron displacement from the Fermi level to the conduction band of the ZnO material, which leads to band gap widening and identification of defects and impurities in ZnO.[43,44] For the CZTS film, an emission band is observed in the visible range centered at 716 nm due to the recombination of electron–hole pairs. Therefore, this CZTS/ZnO heterojunction can work in a broad spectrum. Additionally, to further investigate the durability of the CZTS/ZnO photodetector, a repetitive irradiation test for more than 2500 cycles was carried out under the light of 405 nm at 0.9 mW cm^{-2} illumination without bias voltage (Fig. 4e). Remarkably, the photodetector exhibited high stability and only 10% degradation in sensitivity, indicating that electron–hole pairs could be effectively generated and separated in the CZTS/ZnO heterojunction. This designed photodetector can be utilized in practical applications for maintaining a certain lifetime.

Conclusion

In summary, vertically aligned and highly *c*-axis-oriented ZnO NR arrays and p-type CZTS NCs were employed to construct a nontoxic self-powered CZTS/ZnO heterojunction photodetector with wide spectrum sensitivity ranging from UV to visible light. This CZTS/ZnO photodetector delivers remarkable 31 times higher photocurrent mainly due to the coaxially enhanced photocarrier transportation of the vertically directed ZnO arrays through the nanoconfinement effect along with substantially enhanced incident photon absorption of length-optimized ZnO NRs. Furthermore, this photodetector delivers a high responsivity of 1.1 μA W^{-1}, fast response speed with the response time of 600 ms and recovery time of 600 ms. Evidently, this strategy may provide a new route for designing and constructing materials with superior photocarrier transport in optoelectronic devices and promote the development of highly responsive nontoxic photodetectors for practical applications.

Conflicts of interest

The authors declare no conflict of interest.

Acknowledgements

The authors are thankful to the Analytical and Testing Center of Southwest Jiaotong University for supporting the SEM measurements. This work is supported by the National Natural Science Foundation of China (No. 61801403), the Fundamental Research Funds for the Central Universities of China (A0920502051619-72).

References

1 F. Pelayo García de Arquer, A. Armin, P. Meredith and E. H. Sargent, *Nat. Rev. Mater.*, 2017, 2, 16100.
2 H. Y. Chen, H. Liu, Z. M. Zhang, K. Hu and X. S. Fang, *Adv. Mater.*, 2016, **28**, 403.
3 A. M. Chowdhury, G. Chandan, R. Pant, B. Roul, D. K. Singh, K. K. Nanda and S. B. Krupanidhi, *ACS Appl. Mater. Interfaces*, 2019, **11**, 10418–10425.
4 D. Y. Kim, J. Ryu, J. Manders, J. Lee and F. So, *ACS Appl. Mater. Interfaces*, 2014, **6**, 1370–1374.
5 F. R. Cao, L. X. Meng, M. Wang, W. Tian and L. Li, *Adv. Mater.*, 2019, **31**, 1806725.
6 J. C. Yu, X. Chen, Y. Wang, H. Zhou, M. N. Xue, Y. Xu, Z. S. Li, C. Ye, J. Zhang, P. A. van Aken, P. D. Lundac and H. Wang, *J. Mater. Chem. C*, 2016, **4**, 7302–7308.
7 Z. Zheng, L. Gan, J. B. Zhang, F. W. Zhuge and T. Y. Zhai, *Adv. Sci.*, 2017, **4**, 1600316.
8 H. Liu, X. W. Zhang, L. Q. Zhang, Z. G. Yin, D. G. Wang, J. H. Meng, Q. Jiang, Y. Wang and J. B. You, *J. Mater. Chem. C*, 2017, **5**, 6115–6122.
9 F. Zhang, Y. Ding, Y. Zhang, X. L. Zhang and Z. L. Wang, *ACS Nano*, 2012, **6**, 9229–9236.
10 Z. M. Bai, M. Fu and Y. Zhang, *J. Mater. Sci.*, 2017, **52**, 1308–1317.
11 G. Y. Gou, G. Z. Dai, C. Qian, Y. Liu, Y. Fu, Z. Y. Tian, Y. K. He, L. G. Kong, J. L. Yang, J. Sun and Y. L. Gao, *Nanoscale*, 2016, **8**, 14580–14586.
12 X. D. Mo, X. Li, G. Z. Dai, P. He, J. Sun, H. Huang and J. L. Yang, *Nanoscale*, 2019, **11**, 21386–21393.
13 A. B. Djurisic, X. Y. Chen, Y. H. Leung and A. M. C. Ng, *J. Mater. Chem.*, 2012, **22**, 6526–6535.
14 B. D. Boruah, *Nanoscale Adv.*, 2019, **1**, 2059–2085.
15 T. H. Flemban, M. A. Haque, I. Ajia, N. Alwadai, S. Mitra, T. Wu and I. S. Roqan, *ACS Appl. Mater. Interfaces*, 2017, **9**, 37120–37127.
16 P. Lin, X. Q. Yan, Z. Zhang, Y. W. Shen, Y. G. Zhao, Z. M. Bai and Y. Zhang, *ACS Appl. Mater. Interfaces*, 2013, **5**, 3671–3676.
17 T. Park, K. E. Lee, N. Kim, Y. Oh, J.-K. Yoo and M.-K. Um, *J. Mater. Chem. C*, 2017, **5**, 12256–12263.
18 H. Liu, X. W. Zhang, L. Q. Zhang, Z. G. Yin, D. G. Wang, J. H. Meng, Q. Jiang, Y. Wang and J. B. You, *J. Mater. Chem. C*, 2017, **5**, 6115–6122.
19 C. Wei, J. P. Xu, S. B. Shi, R. Cao, J. Chen, H. Dong, X. S. Zhang, S. G. Yin and L. Li, *J. Mater. Chem. C*, 2019, **7**, 9369–9379.
20 P. Ghamgosar, F. Rigoni, M. G. Kohan, S. J. You, E. A. Morales, R. Mazzaro, V. Morandi, N. Almqvist, I. Concina and A. Vomiero, *ACS Appl. Mater. Interfaces*, 2019, **11**, 23454–23462.
21 W. Wang, M. T. Winkler, O. Gunawan, T. Gokmen, T. K. Todorov, Y. Zhu and D. B. Mitzi, *Adv. Energy Mater.*, 2014, **4**, 1301465.
22 M. T. Winkler, W. Wang, O. Gunawan, H. J. Hovel, T. K. Todorova and D. B. Mitzi, *Energy Environ. Sci.*, 2014, **7**, 1029–1036.
23 A. Walsh, S. Y. Chen, S.-H. Wei and X.-G. Gong, *Adv. Energy Mater.*, 2012, **2**, 400–409.
24 X. Liu, Y. Feng, H. T. Cui, F. Y. Liu, X. J. Hao, G. Conibeer, D. B. Mitzi and M. Green, *Prog. Photovoltaics Res. Appl.*, 2016, **24**, 879–898.
25 J. Li, D. X. Wang, X. L. Li, Y. Zeng and Y. Zhang, *Adv. Sci.*, 2018, **5**, 1700744.
26 S. Giraldo, Z. Jehl, P. Marcel, I.-R. Victor, P. Alejandro and S. Edgardo, *Adv. Mater.*, 2019, 1806692.
27 Z. R. Tian, J. A. Voigt, J. Liu, B. McKenzie, M. J. McDermott, M. A. Rodriguez, H. Konishi and H. Xu, *Nat. Mater.*, 2003, **2**, 821–826.
28 C. F. Pan, J. Y. Zhai and Z. L. Wang, *Chem. Rev.*, 2019, **119**, 9303–9359.
29 F. Zhang, S. M. Niu, W. X. Guo, G. Zhu, Y. Liu, X. L. Zhang and Z. L. Wang, *ACS Nano*, 2013, **7**, 4537–4544.
30 S. Qiao, J. H. Liu, X. N. Niu, B. L. Liang, G. S. Fu, Z. Q. Li, S. F. Wang, K. L. Ren and C. F. Pan, *Adv. Funct. Mater.*, 2018, **28**, 1707311.
31 D. Xiong, W. L. Deng, G. Tian, Y. Y. Gao, X. Chu, C. Yan, L. Jin, Y. H. Su, W. Yan and W. Q. Yang, *Nanoscale*, 2019, **11**, 3021–3027.
32 Q. Yang, X. Guo, W. Wang, Y. Zhang, S. Xu, D. H. Lien and Z. L. Wang, *ACS Nano*, 2010, **4**, 6285–6291.
33 L. F. Hu, J. Yan, M. Y. Liao, H. J. Xiang, X. G. Gong, L. D. Zhang and X. S. Fang, *Adv. Mater.*, 2012, **24**, 2305–2309.
34 V. Q. Dang, T. Q. Trung, D.-I. Kim, L. T. Duy, B.-U. Hwang, D.-W. Lee, B.-Y. Kim, L. D. Toan and N.-E. Lee, *Small*, 2015, **11**, 3054–3065.
35 X. Liu, L. L. Gu, Q. P. Zhang, J. Y. Wu, Y. Z. Long and Z. Y. Fan, *Nat. Commun.*, 2014, **5**, 4007.

36 C. Soci, A. Zhang, B. Xiang, S. A. Dayeh, D. P. R. Aplin, J. Park, X. Y. Bao, Y. H. Lo and D. Wang, *Nano Lett.*, 2007, **7**, 1003–1009.

37 J. J. Hassan, M. A. Mahdi, S. J. Kasim, N. M. Ahmed, H. Abu Hassan and Z. Hassan, *Appl. Phys. Lett.*, 2012, **101**, 261108.

38 Q. Guo, H. W. Hillhouse and R. Agrawal, *J. Am. Chem. Soc.*, 2009, **131**, 11672–11673.

39 J. Xu, Z. Q. Hu, J. J. Zhang, W. Xiong, L. L. Sun, L. Wan, R. Zhou, Y. Jiang and C.-S. Lee, *J. Mater. Chem. A*, 2017, **5**, 25230–25236.

40 S. Ji, T. Shi, X. Qiu, J. Zhang, C. Chen, Z. Jiang and C. Ye, *Sci. Rep.*, 2013, **3**, 2733.

41 K. Tanaka, N. Moritake and H. Uchiki, *Sol. Energy Mater. Sol. Cells*, 2007, **91**, 1199–1201.

42 A. Umar, C. Ribeiro, A. Al-Hajry, Y. Masuda and Y. B. Hahn, *J. Phys. Chem. C*, 2009, **113**, 14715–14720.

43 S. S. Liu, M.-Y. Li, D. Su, M. N. Yu, H. Kan, H. Liu, X. Wang and S. L. Jiang, *ACS Appl. Mater. Interfaces*, 2018, **10**, 32516–32525.

44 M.-Y. Li, M. N. Yu, D. Su, J. B. Zhang, S. L. Jiang, J. Wu, Q. P. Wang and S. S. Liu, *Small*, 2019, **15**, 1901606.